Different models of the Mars solar wind interaction: Implications for ENA imaging

H. Gunell, M. Holmström, S. Barabash, E. Kallio, P. Janhunen, A. F. Nagy and Y. Ma

INSTITUTET FÖR RYMDFYSIK
Swedish Institute of Space Physics

Kiruna, Sweden

Different models of the Mars solar wind interaction: Implications for ENA imaging

H. Gunell, M. Holmström, and S. Barabash
Swedish Institute of Space Physics, Kiruna, Sweden

E. Kallio and P. Janhunen
Finnish Meteorological Institute, Helsinki, Finland

A. F. Nagy and Y. Ma
University of Michigan, Ann Arbor, Michigan, USA

Abstract

In this report energetic neutral atom (ENA) images that are calculated from plasma parameters given by three different simulation models of the interaction between the solar wind and Mars are presented and compared. The ENA images are calculated by combining a model for the ion flow and temperature with a model of the neutral atmosphere using the cross sections for the charge exchange collisions. The three ion models are: an empirical model that is based on Phobos 2 measurements; a three-dimensional hybrid simulation; and a three-dimensional MHD simulation. For the empirical and MHD models the ENA images are obtained by integration of the ENA emission along lines of sight to a virtual ENA instrument. In the case of the hybrid model ENA images are obtained by summing the contributions from all ions, whose positions, velocities, and weights are saved in files at regular intervals.

It is found that the magnetic pileup boundary can be seen in the ENA images that are based on models where such a boundary is present, i.e. the empirical and MHD models. Asymmetries in the proton and oxygen ion densities develop in the hybrid model and can be seen in the hydrogen and oxygen ENA images respectively.

This study shows the importance of considering not only the type of simulation model used, but also the proper inclusion of relevant physical phenomena and boundary conditions, when modelling the interaction between planets and the solar wind.

Herbert Gunell
Swedish Institute of Space Physics
P.O. Box 812
SE-981 28 Kiruna
Sweden
herbert.gunell@physics.org

Contents

Preface

Imaging of energetic neutral atoms (ENAs) is an interesting diagnostic tool for the study of the interaction between the solar wind and planetary atmospheres. ENA detecting instruments will fly to Mars on ESAs Mars Express mission in 2003 and to Venus on the Venus Express spacecraft in 2005. To aid the interpretation of the ENA images, and to understand the physics behind them, models that are able to produce simulated ENA images play an important role. This report describes a comparative study of three different models of the interaction of the solar wind and Mars, showing some differences between the models and pointing out a few aspects of modelling that are important for ENA imaging. With the development of scientific computing, and the increasing speed and memory capabilities of modern computers an improvement, both in detail and accuracy, of the models of the solar wind–planetary interaction is expected in the not too distant future, and that will certainly also affect the simulated ENA images.

Kiruna, 7 August 2003

Herbert Gunell

1 Introduction

Three different models of the interaction between the solar wind and Mars have been examined in this report, with emphasis on the generation of ENA images. The three models are:

1. an empirical model that is based on Phobos 2 measurements [1],

2. a three dimensional hybrid simulation [2, 3], and

3. a three-dimensional MHD simulation [4].

Hydrogen ENA images from the empirical model were computed and published by Holmström, et al., [5]. They calculated the ENA emission by combining the empirical model of the plasma flow with a model for the neutral gas density of the Martian atmosphere, using cross sections for the relevant charge exchange reactions. The ENA images are then generated by integrating the ENA emission along lines of sight to a virtual ENA instrument. This approach does not self-consistently account for the loss of ions when ENAS are produced. A similar approach was used by Barabash, et al., [6] to generate oxygen ENA images; the difference being that the flow of oxygen ion was given by a test particle simulation, where trajectories of oxygen ion test particles moving in the electric and magnetic fields of the empirical model were calculated.

ENA images from the MHD model are generated in the same way as with the empirical model. The flows of hydrogen and oxygen ions are given by the output of the MHD code and these are combined with the models of the neutral gas densities and cross sections. Fig. 1 shows an example of the plasma flow, and Fig. 2 shows the neutral gas density as a function of altitude. The number density n_i of neutral species i is modelled as

$$n_i = N_i e^{-\beta_i \left(\frac{1}{r_0} - \frac{1}{r} \right)} \zeta(\beta_i/r) \tag{1}$$

where r is the distance to the centre of Mars, r_0 is the radius of the exobase, ζ is Chamberlain's partition function [7], and β_i is a constant that is set by the mass and temperature of each species

$$\beta_i = \frac{GMm_i}{k_B T_i} \tag{2}$$

where G is the gravitational constant, $M = 6.46 \cdot 10^{23}$ kg is the mass of Mars, m_i is the atomic mass of neutral species i, and T_i is the temperature of species i at the exobase. The parameters have been adopted from references [1, 5, 8]. An exobase altitude of 170 km is used throughout this report. The other parameters are shown in Table 1.

The hybrid code is able to generate its own discrete ENAs since the position and velocity of all super-ions are known at each time step. The probability for an ion to have a charge exchange collision is then found from the neutral density and the energy dependent cross section. The weight of the super-ion is reduced in proportion to the probability of a charge exchange collision. Charge exchange collisions are thus
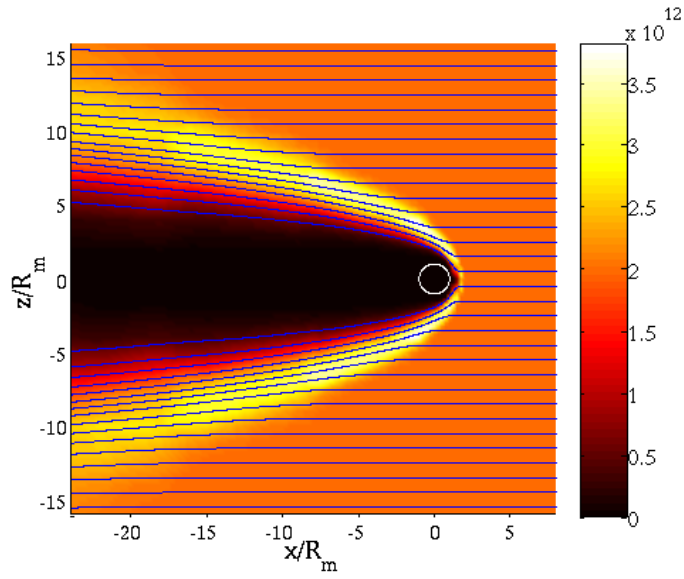
Figure 1: Plasma flow around Mars in the MHD model shown in the $y = 0$ plane. The blue lines are stream lines, and the colour scale shows the proton flux in units of $\mathrm{m}^{-2}\mathrm{s}^{-1}$.
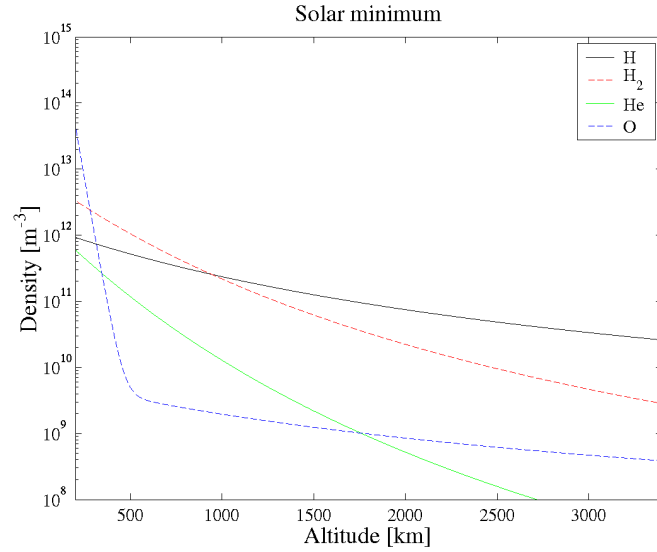

Figure 2: Neutral gas densities as a function of altitude for the dominant neutral species in the upper atmosphere of Mars. Of these H, H_2, and O are important for the generation of energetic neutral atoms. The contribution from helium is negligible because of its very small cross section for charge exchange collisions.

Table 1: Parameters of the neutral gas density model [1, 5, 8]. The exobase is located at 170 km altitude.

Species	N_i	T_i
H	$9.9 \cdot 10^{11}$ m^{-3}	192 K
H$_2$	$3.8 \cdot 10^{12}$ m^{-3}	192 K
He	$7.2 \cdot 10^{11}$ m^{-3}	275 K
O$_{hot}$	$5.5 \cdot 10^{9}$ m^{-3}	$4.4 \cdot 10^3$ K
O$_{thermal}$	$1.4 \cdot 10^{14}$ m^{-3}	173 K

Table 2: Solar wind parameters

Plasma density	$4 \cdot 10^6$m^{-3}	
Temperature	$1.75 \cdot 10^5$K	(mean of $5 \cdot 10^4$ K protons and $3 \cdot 10^5$ K electrons)
Solar wind speed	500 km/s	
Magnetic flux density	3 nT	direction: $(x, y, z) = (cos(56°), sin(56°), 0)$

accounted for self-consistently. The super-ion velocities, positions, and weights are saved periodically, and the images are generated when the simulation has been run by computing the trajectories of the super-ENAs and collecting them with a virtual ENA instrument.

The solar wind parameters that are used throughout this report follow those used by Ma, et al., [4] as closely as possible, and are shown in Table 2. The neutral gas densities used when computing the ENA images are shown in Fig. 2. The coordinate system that is used in this report has its origin in the centre of Mars, the sun in the positive x-direction, the z-axis is northernly directed and perpendicular to the ecliptic. The y-direction closes the right-handed system.
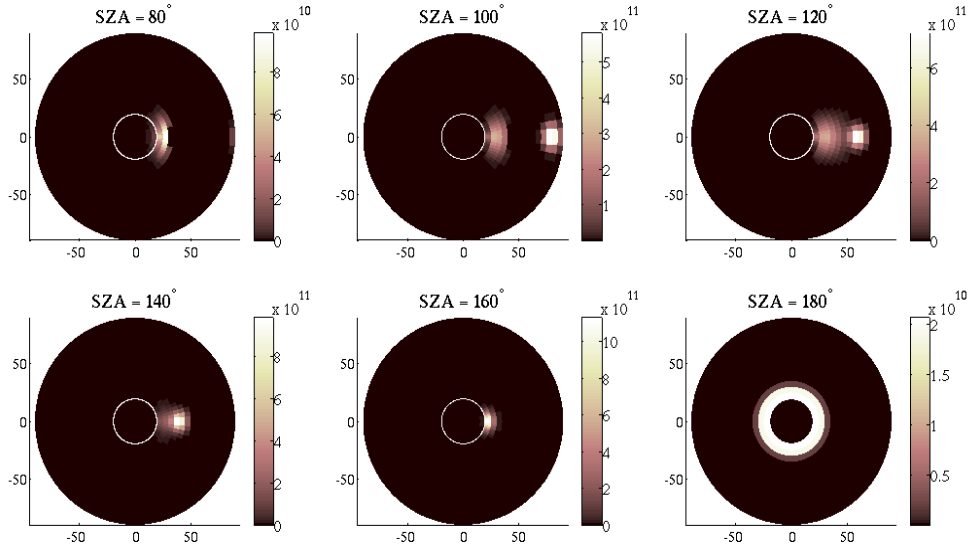
Figure 3: Hydrogen ENA-images from the empirical model. The ENA images shown are from vantage points $3R_m$ from the centre of Mars, looking down at the planet. The solar zenith angles are, from left to right starting in the upper row; $80°$, $100°$, $120°$, $140°$, $160°$, and $180°$. The ENA flux is shown in units of $\text{sr}^{-1}\text{m}^{-2}\text{s}^{-1}$.

2 The empirical model

2.1 Introduction

An empirical model for the plasma flow around Mars based on measurements made with the ASPERA instrument on board the Phobos 2 spacecraft was developed by Kallio [9]. This model was used to study the production of energetic neutral atoms through charge exchange collisions between the solar wind protons and atoms and molecules in the Martian neutral atmosphere [1]. ENA images based on this model have been calculated for both hydrogen [5] and oxygen [6] ENAs. The model is cylindrically symmetric with respect to the Mars-sun axis, and includes a bow shock and a magnetic pileup boundary. The model is parameterised, and the parameter values used here are the same as those used in reference [5].

2.2 Hydrogen ENA images

The ENA images were calculated by integrating the ENA production along lines of sight as described by Holmström, et al. [5]. Fig. 3 shows hydrogen ENA images from vantage points in the $x-z$-plane, three Mars radii (R_m) away from the centre of Mars. Due to the cylindrical symmetry of the model the images from any vantage points with the same solar zenith angle and planetocentric distance are identical. The structure and shape of the images are in reasonable agreement with the MHD model, although the absolute values of the ENA flux are slightly lower in the images

produced by the empirical model. There are two maxima in the ENA flux; one produced upstream in the solar wind and another closer to, but separated from, the planet. The ENAs that are produced in the solar wind are dominating in those of the images where the direction of the sun is within the range of polar angles shown. This is because we are then looking directly into the solar wind flow. When the plasma flow is not directed straight at our virtual instrument we only collect ions moving at an angle to the flow velocity due to the plasma temperature. The length of the integration path is also an issue related to the magnitude of the computed ENA flux. For the empirical model the ENA production is integrated inside a sphere of radius $20R_m$ centred at Mars. The proton temperature is given by an analytical approximation from gas dynamics [1].

The images were obtained by integrating along lines of sight from a virtual ENA instrument. A Maxwellian velocity distribution of the solar wind protons was assumed.

2.3 Oxygen ENA images

The oxygen ion distribution function has been estimated by a test particle simulation [6]. The test particles move under the influence of the solar wind magnetic field and the induced electric field $\vec{E} = -\vec{v} \times \vec{B}$, assuming frozen-in field lines, and the flow velocity being given by the empirical flow model [9]. The trajectories of the ions are calculated and from those the six-dimensional distribution function is calculated in a simulation box that in physical space is $4R_m \times 4R_m \times 4R_m$ and centred on Mars. The source, giving the initial distribution, of O^+ test particles was photo-ionised oxygen.

With knowledge of the O^+ distribution function, the neutral gas density profiles in the vicinity of Mars and the cross sections for charge exchange the ENA emission can now be calculated. The ENA images are then obtained by integration of the ENA emission along lines of sight. Since the number of points in velocity space where the distribution function is known is relatively small it is difficult to accurately integrate over energy. An estimate can be made, however, and it is shown in Fig. 4, which includes the contribution from oxygen ENAs with energies over 100 eV. The figure shows oxygen ENA images from vantage points in the $x - z$-plane, three Mars radii away from the centre of Mars. Fig. 5 shows the logarithm of the ENA flux that is shown in Fig. 4.

2.4 ENA production

The production rate for hydrogen ENAs is shown in Fig. 6. The production rate has been integrated over the azimuthal coordinate. In the empirical model the maximum is located about one Mars radius off the x-axis, and the ENA production on the x-axis above the sub-solar point is small. The maximum in the ENA production is clearly separated from the planet, a fact that also can be seen in the ENA images (Fig. 3). As we shall see in the next section this is not true for all models.
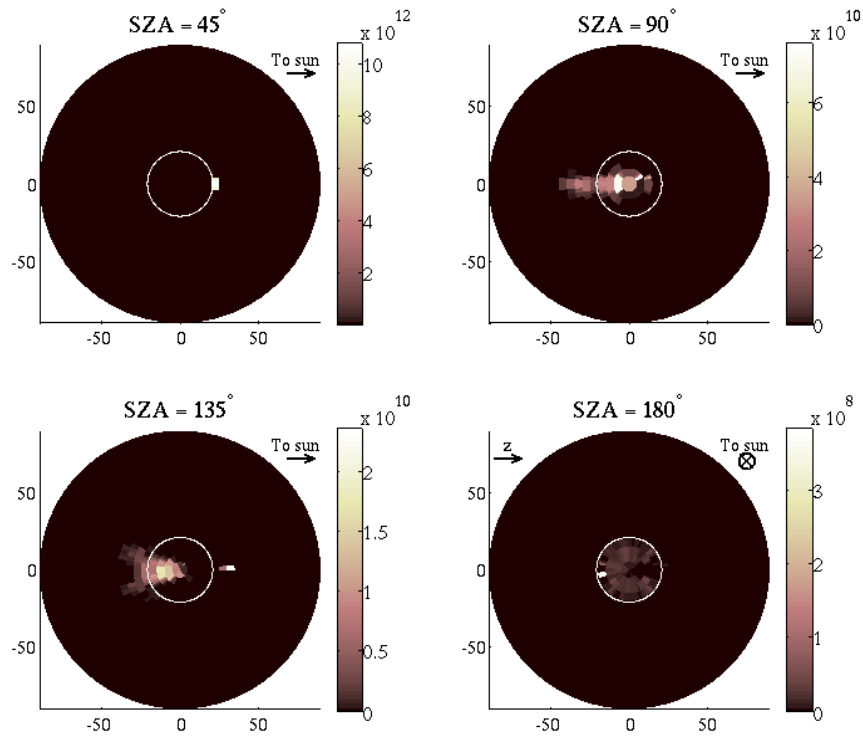
5

Figure 4: Oxygen ENA-images from the empirical model. The images shown are from vantage points in the $x - z$-plane $3R_m$ from the centre of Mars, looking down at the planet. The solar zenith angles are $45°$, $90°$, $135°$, and $180°$. The ENA flux is shown in units of $\text{sr}^{-1}\text{m}^{-2}\text{s}^{-1}$.
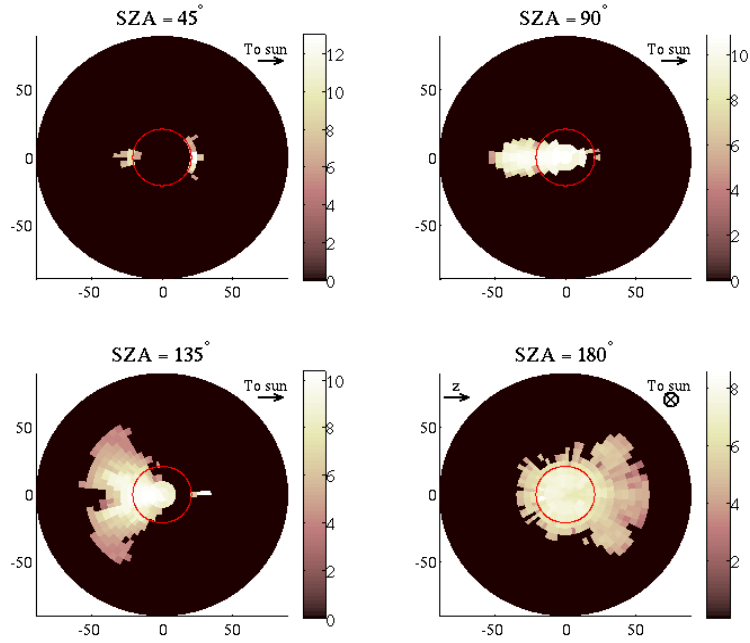
Figure 5: Oxygen ENA-images from the empirical model. These images show the logarithm of the ENA flux shown in Fig. 4.
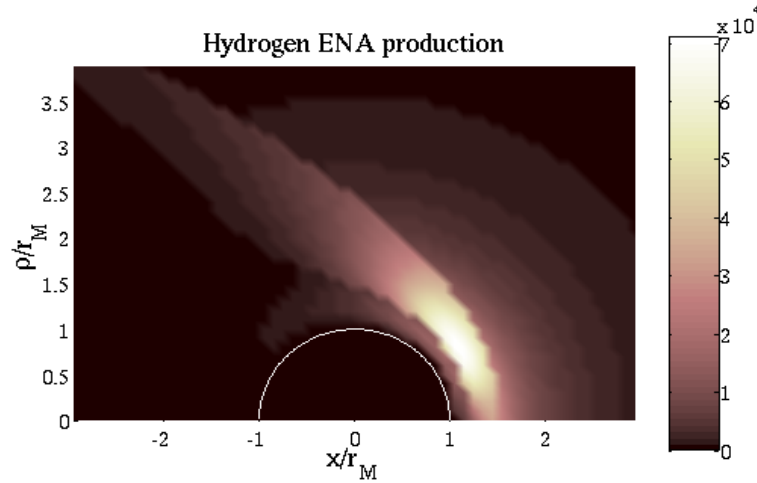

Figure 6: Production of hydrogen ENAs in the empirical model. The colour-coded production rate has been integrated over the azimuthal angle, and is given in units of $m^{-3}s^{-1}$. The cylindrical coordinate $\rho = \sqrt{y^2 + z^2}$ is the distance from the Mars–sun line.

7

3 The hybrid simulation

3.1 The model

We now investigate the results of a run of the three-dimensional hybrid simulation code developed by Kallio and Janhunen [2, 3]. The simulation is performed on a $30 \times 30 \times 30$-grid with a uniform grid spacing of 720 km $\approx 0.2R_m$. This is probably the reason why the magnetic pileup boundary is not seen in the hybrid simulation. It is unlikely that it can be resolved on such a coarse grid. There are three different ion species included in the simulation; H^+, O^+, and O_2^+. The number of super-particles per grid cell is about 15, but it can vary for the different ion species.

The hybrid code self-consistently includes four charge exchange reactions, namely

1. $H^+ + O \rightarrow H + O^+$,

2. $O^+ + O \rightarrow O + O^+$,

3. $H^+ + H \rightarrow H + H^+$, and

4. $O^+ + H \rightarrow O + H^+$.

How significant the loss of solar wind protons due to charge exchange collisions is to the solar wind flow around Mars remains to be seen, and could be studied by varying the neutral densities in the simulation.

3.2 Density distribution

Barabash, et al., [6] used a test particle simulation with $\vec{E}$- and $\vec{B}$-fields from the empirical model to calculate column densities, i.e., densities integrated across the simulation box along one of the coordinates, and found a maximum of the oxygen ion density above the northern hemisphere (or the $+\vec{E}_{sw}$ hemisphere, since the solar wind electric field is northernly directed). In the published run of this hybrid simulation code [3], as well as in the run presented here, the maximum O^+ density is on the southern side of Mars, i.e. on the $-\vec{E}_{sw}$ side. Fig. 7 shows the O^+ density in the $x - z$-plane of the hybrid simulation. The density has its maximum on the southern side of the planet. This is most evident on the nightside, where a large southernly region of high O^+ density can be seen.

In the hybrid simulation there is an emission of O^+ ions from the ionosphere of $1.4 \cdot 10^{25}$ oxygen ions per second, and a $2 \cdot 10^{25} s^{-1}$ emission of O_2^+. There is no such emission in the test particle simulation of oxygen ions in the fields produced by the empirical model [6].

This provides an explanation of the discrepancy that is consistent with the observations, because ions that are emitted in the direction of the electric field are quickly accelerated away, only making a small contribution to the density on the northern $(+\vec{E}_{sw})$ side. Ions emitted from the southern $(-\vec{E}_{sw})$ side of the ionosphere, on the other hand, are decelerated by the electric field and having lower speed contribute more to the density on the southern side of Mars, before eventually escaping the planet or turning back to be reabsorbed by the ionosphere.
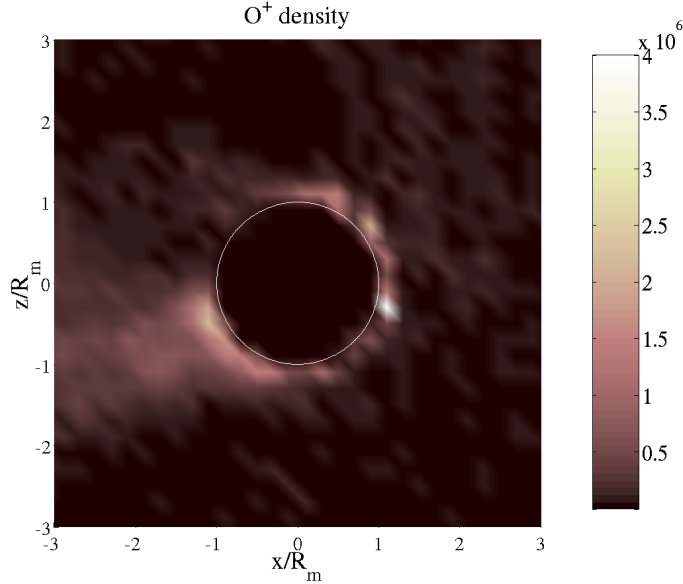
Figure 7: O^+ density in the $x - z$-plane for the the hybrid code. Oxygen ions that are emitted from the ionosphere, are the likely cause for the position of the O^+ density maximum. The density is shown in units of m^{-3}.

When, as in the empirical model [6], no ionospheric source is present the O^+ density close to the planet is determined by loss of ions to precipitation, which is higher on the $-\vec{E}_{sw}$ side, where oxygen ions are accelerated toward the planet by the electric field.

3.3   ENA images

The positions, velocities and weights of all super-particles in the simulation are periodically saved in files every five seconds starting at time $t = 200$ s and ending at $t = 245$ s, when ten files have been saved. Knowing the neutral gas densities and the energy dependent charge exchange cross sections the ENA production rate for each super ion can easily be calculated. The number of ENAs per second generated by the ith proton is

$$q_i = w_i v_i \sum_\alpha N_\alpha(\vec{r}_i)\sigma_\alpha(v_i) \tag{3}$$

where w_i is the number of real protons that are represented by super-proton i, $N_\alpha(\vec{r}_i)$ is the density of neutral gas species α at the position $\vec{r}_i$ of proton i, and $\sigma_\alpha(v_i)$ is the cross section for charge exchange collisions between a proton with speed v_i and a neutral particle of species α.

The newly produced ENAs are assumed to travel with the same velocity as the incident ion, and those that hit a virtual ENA detector are collected in bins
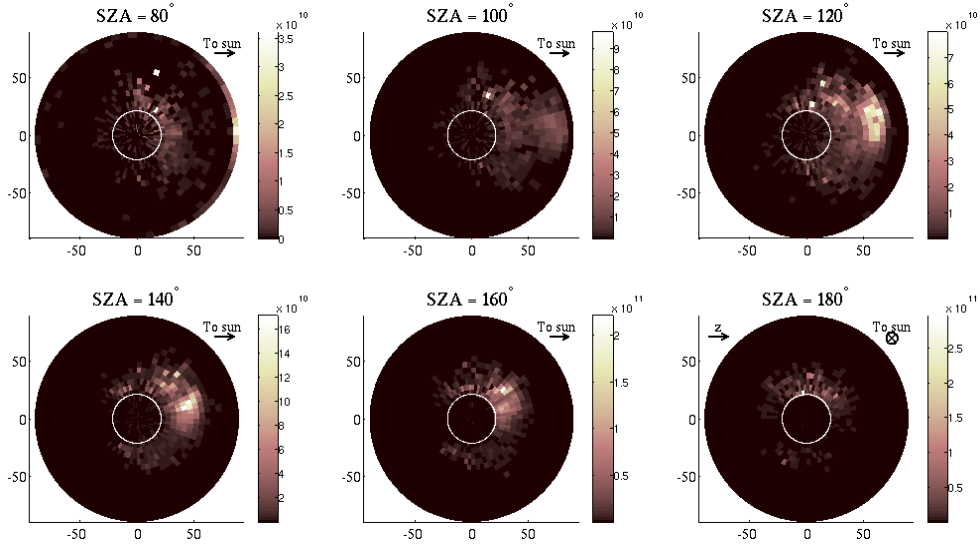
9

Figure 8: Hydrogen ENA-images produced by the hybrid model. Mars is viewed from vantage points in the $x - z$-plane three Martian radii from the centre of Mars. From left to right, starting at the upper left panel, the solar zenith angles of the vantage points are $80°, 100°, 120°, 140°, 160°,$ and $180°$. The ENA flux is shown in units of $\text{sr}^{-1}\text{m}^{-2}\text{s}^{-1}$.

depending on their respective incident angles. For the pictures presented here the radius of the "ENA camera" is $0.2R_m$ for the hydrogen images and $0.5R_m$ for the oxygen images. The larger radius in the oxygen case is necessary due to the smaller number of oxygen super-particles. Finally the images from the ten dump files are averaged.

An obstacle boundary at 3700 km planetocentric distance has been assumed when calculating the ENA images. This is because the number of super-particles inside that boundary is so small in the simulation that including those would produce unrealistic results. The number density of super-particles must not be to small or else the particle discreteness will produce a spotty picture. If this happens in a region with low neutral density the error is not significant, since then the produced ENA flux is small anyway, but inside 3700 km the neutral density is high and there is a significant ENA production.

Hydrogen ENA images generated from the same vantage points as the images published by Holmström, et al., [5] are shown in Fig. 8. The hydrogen ENA images include ENAs with energies over 50 eV. A local maximum on the right hand side of the pictures representing ENAs produced upstream in the solar wind can be seen. The contribution from the solar wind upstream of the bow shock is smaller in the hybrid model than in the other two models because of the size of the simulation box. It only reaches three Mars radii from the centre of mars in the x-direction, and thus the contributions from charge exchange reactions taking place further away are
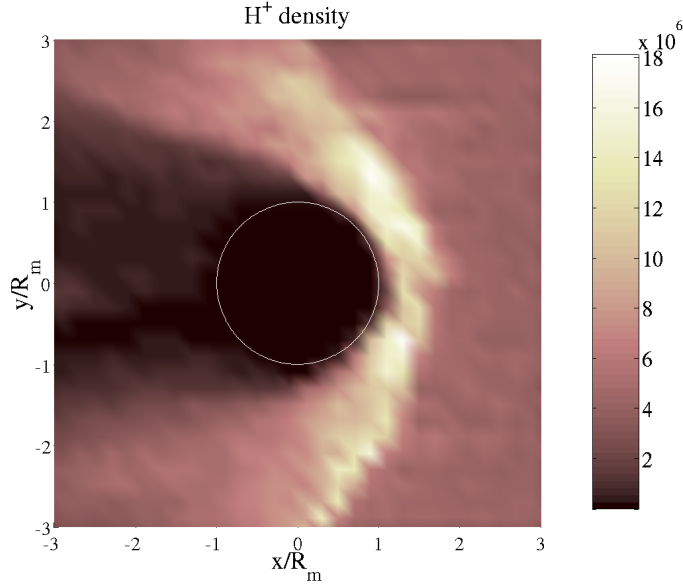
10

Figure 9: H$^+$ density in the $x-y$-plane. The asymmetry between the dawn and dusk sides can also be spotted in the hydrogen ENA images (Fig. 8). The density is shown in units of m^{-3}.

not included. In the MHD simulation the simulation box goes out to $x = 8R_m$, and in the empirical model the integration is performed out to twenty Mars radii. The other (main) maximum is not separated from the planet, which probably is due to the absence of a magnetic pileup boundary in this model.

There is also an asymmetry with respect to the Mars-sun axis in the hydrogen ENA images in Fig. 8. The ENA emission is larger from the upper part of the images, corresponding to the dusk-side of Mars. This is most likely a result of an asymmetry in the proton density, which is shown in Fig. 9.

Fig. 10 shows oxygen ENA images, including oxygen ENAs with energies exceeding 100 eV. The asymmetry in the oxygen images is a result of the asymmetry in the O$^+$ density. This is most easily seen from the lower right panel of Fig. 10, where the vantage point is above the anti-solar point. Since the asymmetry in the ion density can be seen in the oxygen ENA image, such images can be used to remotely measure asymmetries in the global distribution of oxygen ions.

3.4   ENA production

The production rate for hydrogen ENAs is shown in Fig. 11. The production rate has been integrated over the azimuthal coordinate. In the hybrid simulation considered here the maximal production rate appears on the x-axis on the dayside of Mars, whereas in the empirical model the maximum is located about one Mars radius off axis, c. f., Fig. 6.
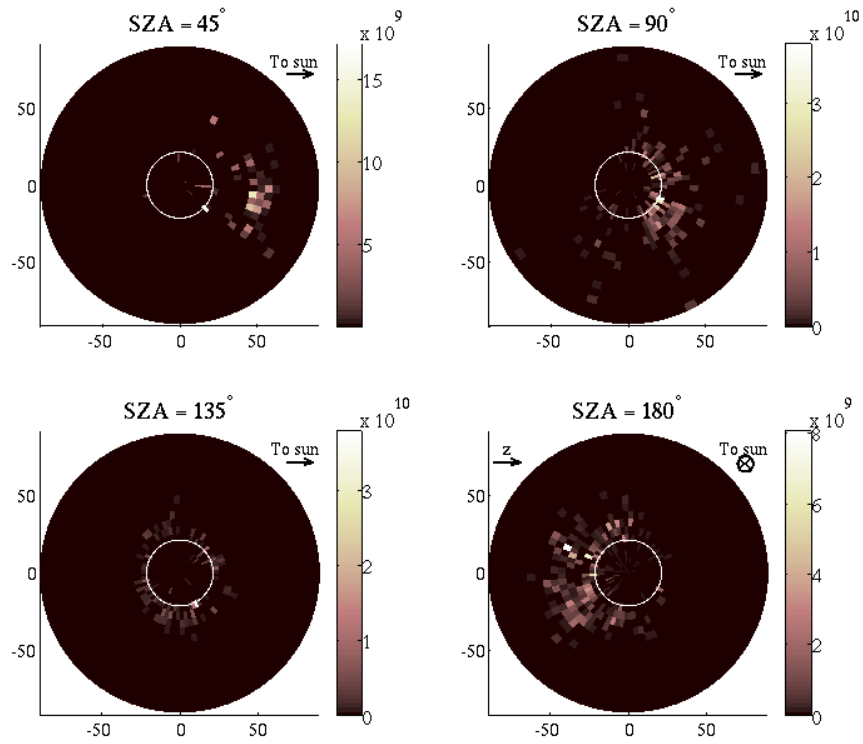
11

Figure 10: Oxygen ENA-images from the hybrid model. Mars is viewed from a vantage point in the $x-z$-plane, three Martian radii from the centre of Mars. From left to right, starting at the upper left panel, the solar zenith angles of the vantage points are $45°$, $90°$, $135°$, and $180°$. The ENA flux is shown in units of $\mathrm{sr}^{-1}\mathrm{m}^{-2}\mathrm{s}^{-1}$.
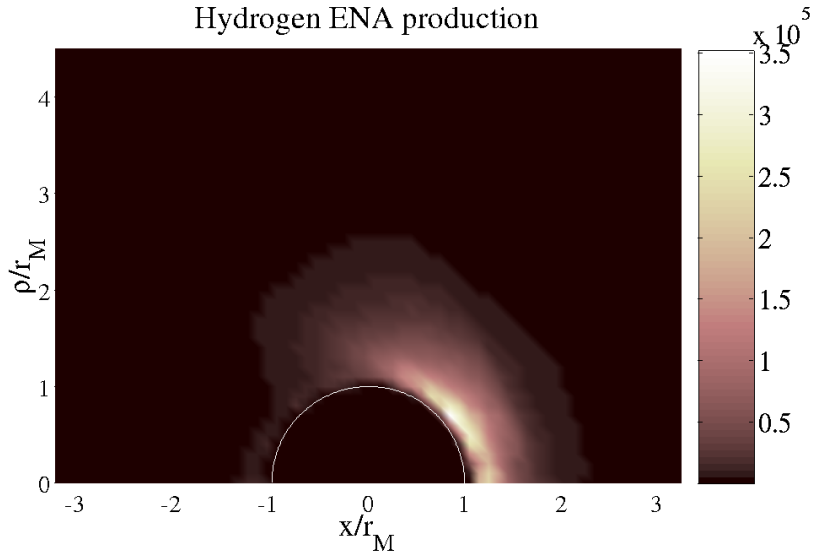
12

Hydrogen ENA production

Figure 11: Production of hydrogen ENAs in the hybrid model. The production rate has been integrated over the azimuthal angle, and is given in units of $\mathrm{m}^{-3}\mathrm{s}^{-1}$. The cylindrical coordinate $\rho = \sqrt{y^2 + z^2}$ is the distance from the Mars–sun line.

Apart from reaching the axis rather than being annular the production region in the hybrid simulation also shows a production rate almost ten times higher than the production rate in the empirical model. Compared with the empirical model the ENA production maximum is much closer to the planet in the hybrid model. Whether this is a result of the coarse grid used in the hybrid simulation or there are other reasons is at this point not entirely clear.
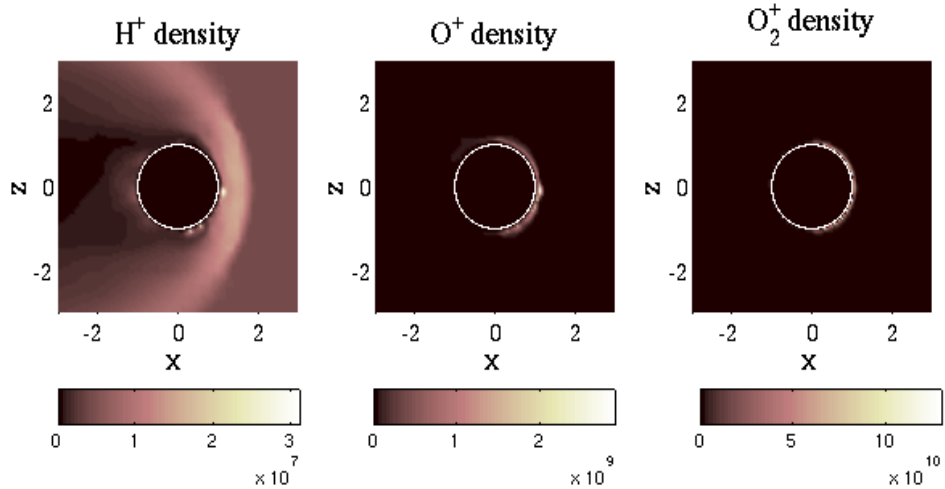
Figure 12: Densities in the $x - z$-plane of the MHD model for the protons (left panel), O^+ ions (middle panel), and O_2^+ ions (right panel). The number density is shown in units of m^{-3}.

4 The MHD simulation

4.1 The model

The ENA images presented in this section are based on the ion flow results obtained from an MHD simulation by Ma, et al.[4]. One momentum equation that includes separate densities for the three different ion species, namely H^+, O_2^+, and O^+, is considered in their model. Source and loss terms are included for O_2^+ and O^+, but not for H^+. The simulation box is defined by $-24R_m \leq x \leq 8R_m$, $|y| \leq 16R_m$, $|z| \leq 16R_m$. The grid is nonuniform with a grid size of $2R_m$ far from the planet on the nightside, and as small as $R_m/64$ close to the planet.

The crustal magnetic fields of Mars were taken included in the simulations by the use of a 60-degree expansion based on Mars Global Surveyor data [10]. The inclusion of the crustal magnetic fields is seen to affect the location of the ionopause [4].

4.2 Density distribution

Fig. 12 shows the densities in the $x - z$-plane for the protons (left panel), O^+ ions (middle panel), and O_2^+ ions (right panel). The MHD simulation resolves much higher O^+ and O_2^+ densities close to the Martian surface than the hybrid code does, and hence the middle and left panels of Fig. 12 are dominated by the region closest to the planet. Fig. 13 shows the O^+ ion density in the $x - z$-plane on the nightside of Mars. A slightly higher density can be seen on the northern $(+\vec{E}_{sw})$ side, that is opposite to the hybrid simulation which has its maximum on the $-\vec{E}_{sw}$ side.
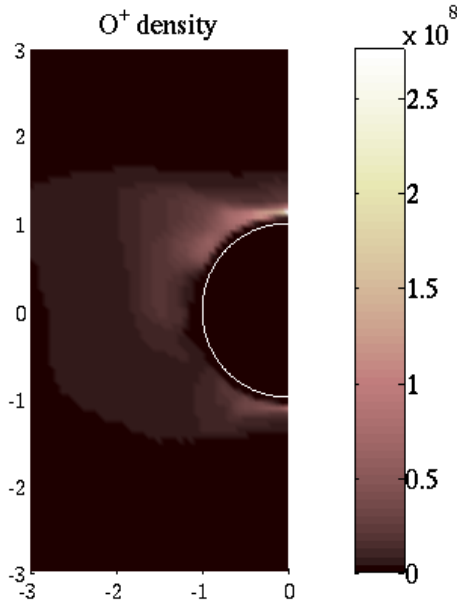
14

Figure 13: The O^+ ion density of the MHD model shown in the $x-z$-plane on the nightside of Mars. The number density is shown in units of m^{-3}.

However, the asymmetry is smaller here than in the hybrid case. The difference between the models in this respect is probably due to the absence of an ionospheric emission of O^+ and O_2^+ ions in the MHD model.

4.3 ENA images

The ENA images from the MHD model were calculated in the same way as those of the empirical model described in section 2.2 and in detail in reference [5]. The plasma flow and temperature values are obtained from the output files from the run of the MHD code. When evaluating the line of sight integrals linear interpolation of the values known at the grid points is performed. In the hydrogen and oxygen images ENAs with energies exceeding 50 eV and 100 eV respectively are included. Fig. 14 shows hydrogen ENA images from vantage points in the $x-z$-plane, three Mars radii away from the centre of Mars, and with solar zenith angles $80°$, $100°$, $120°$, $140°$, $160°$, and $180°$. In the first panel the solar zenith angle is $80°$ and two local maxima in the ENA flux can be seen. The maximum at the right hand side of the figure represents ENAs produced in the solar wind. There is also a local maximum close to, but separated from, the planet. As the vantage point is moved toward the nightside of Mars in the subsequent panels the maximum associated with ENAs produced upstream in the solar wind moves toward the centre of the image and is dominating over the other maximum. That the maximum ENA flux is separated from the planet
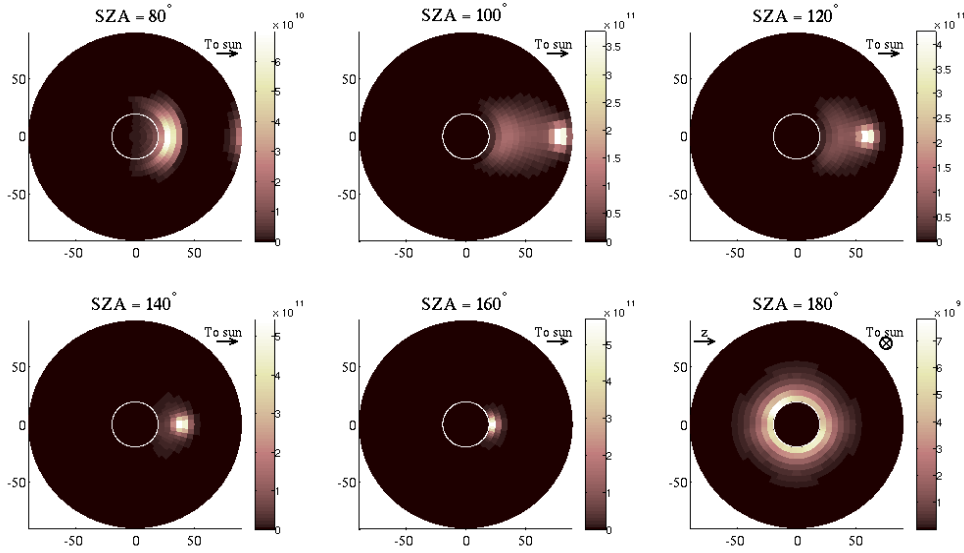
15

Figure 14: Hydrogen ENA-images produced by the MHD model. Mars is viewed from a vantage point in the $x - z$-plane, three Martian radii from the centre of Mars. From left to right, starting at the upper left panel, the solar zenith angles of the vantage points are $80°$, $100°$, $120°$, $140°$, $160°$, and $180°$. The ENA flux is shown in units of $sr^{-1}m^{-2}s^{-1}$.

shows that the magnetic pileup boundary that appears in the MHD simulation also can be detected in ENA images. This should be compared to the hybrid simulation (Fig. 8), where no magnetic pileup boundary can be seen. There are thus differences between the models that spacecraft-based ENA instruments should be able to detect.

Fig. 15 shows oxygen ENA images from vantage points in the $x - z$-plane, three Mars radii away from the centre of Mars, and solar zenith angles $45°$, $90°$, $135°$, and $180°$. In comparison with the hybrid model (Fig. 10) the oxygen ENA images from the MHD model are completely different. In the images from solar zenith angles $45°$ and $90°$ the maximum ENA flux show up on opposite sides of Mars in the two models, and for SZA=$135°$ the maximum is on the sunward side of Mars in the MHD model and the hybrid model shows no clear maximum. It is possible that these differences could be explained by the asymmetry of the O^+ ions in the hybrid model and the absence of such an asymmetry in the MHD model. A more detailed study of the to models would, however, be needed to say anything conclusively.

The image from SZA=$180°$ shows maxima both north and south of the planet of approximately the same intensity, which is consistent with the MHD model having only a small north-south asymmetry in the oxygen ion density. The corresponding image from the hybrid model shows an asymmetry which is consistent with the asymmetrical oxygen ion density distribution of that model.
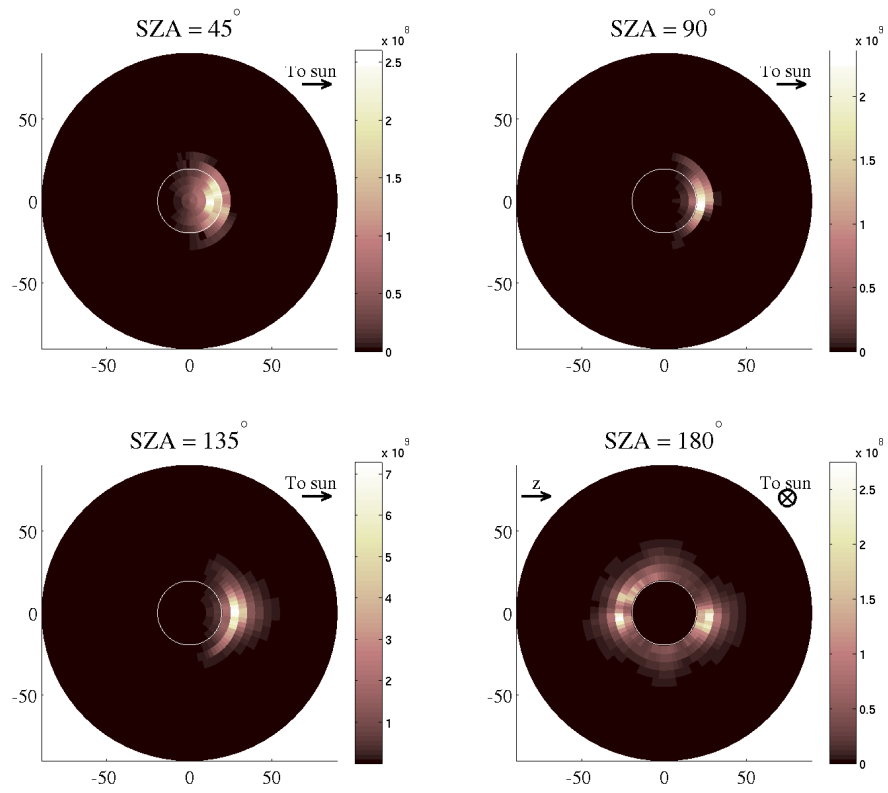
16

Figure 15: Oxygen ENA-images from the MHD model. Mars is viewed from a vantage point in the $x - z$-plane, three Martian radii from the centre of Mars. From left to right, starting at the upper left panel, the solar zenith angles of the vantage points are $45°$, $90°$, $135°$, and $180°$. The ENA flux is shown in units of $sr^{-1}m^{-2}s^{-1}$.
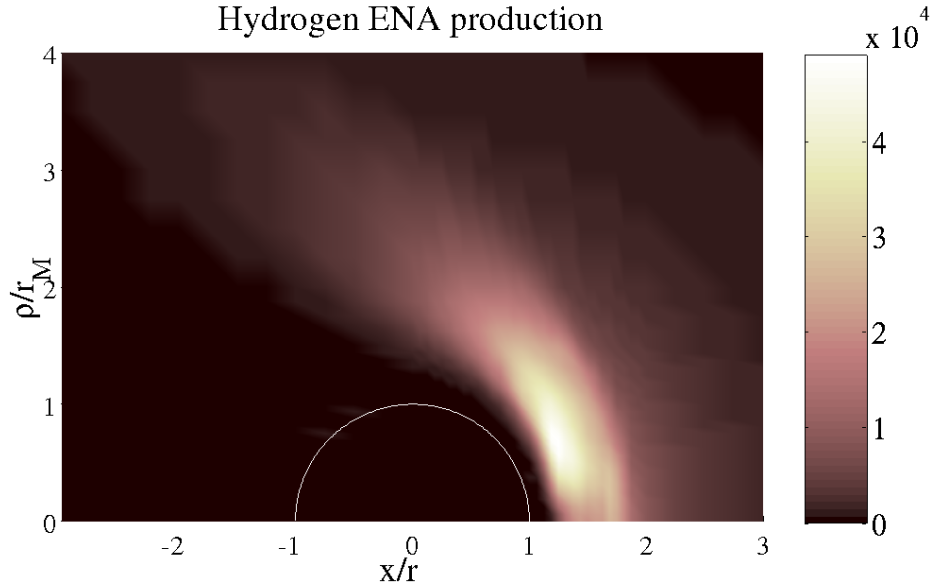
Figure 16: Production of hydrogen ENAs. The production rate, which has been integrated over the azimuthal angle, is given in units of $m^{-3}s^{-1}$. The cylindrical coordinate $\rho = \sqrt{y^2 + z^2}$ is the distance from the Mars–sun line.

4.4 ENA production

The production rate for hydrogen ENAs is shown in Fig. 16. The production rate has been integrated over the azimuthal coordinate for comparison with the results of the other models. The highest production rate in the MHD model (Fig. 16) is approximately equal to the highest production rate in the hybrid model (Fig. 11) and is thus about four times higher than the production rate in the empirical model. The global maximum is located off the Mars-sun line like it is in the empirical model, however a significant production rate is found on the Mars-sun line like it is in the hybrid model. The region with a high ENA production rate is located further away from the planet in the MHD than in the hybrid model, probably due to the presence of a magnetic pileup boundary in the MHD results.

Table 3: A comparison of some aspects of the results of the different models. The solar wind hydrogen ENA flux are taken from the images with a solar zenith angle of $100°$.

	Empirical	Hybrid	MHD	unit
Solar wind H-ENA flux	$5.8 \cdot 10^{11}$	$2.0 \cdot 10^{10}$	$3.8 \cdot 10^{11}$	$\text{sr}^{-1}\text{m}^{-2}\text{s}^{-1}$
Total H-ENA production	$2.7 \cdot 10^{25}$	$5.5 \cdot 10^{25}$	$2.4 \cdot 10^{25}$	s^{-1}
Magnetic pileup boundary	Yes	No	Yes	

5   Summary and conclusions

We have simulated ENA images based on three different models of the plasma flow around Mars. Fig. 17 shows three ENA images from each model. These images are the images from solar zenith angles $100°$, $140°$, and $180°$ that are also shown in figures 3, 8, and 14. In Fig. 17 the left column shows ENA images from the empirical model, the middle column the hybrid model, and the right column shows ENA images from the MHD model. The colour scales are the same for panels on the same row to enable a quantitative comparison between the models.

It can be seen in the top row, where the solar zenith angle is $100°$, that the observed flux of ENAs produced in the solar wind is lowest in the hybrid model. This, as has been pointed out in previous sections, is a result of the smaller simulation box used in that model. It can also bee seen that the upstream maximum is about 50 % stronger in the empirical (top left panel) than in the MHD model (top right panel). The reason for this is yet unknown, but one possibility is that the ENA flux is influenced by the bow shock position and the discretisation of the images.

From the bottom row in Fig. 17 it is seen that the hybrid model produce a much larger ENA flux than the other models when Mars is viewed from the nightside. This could be a result of kinetic effects that are absent in the empirical and MHD models.

The hybrid model does not produce a magnetic pileup boundary, when run with the present parameters and a grid size of 720 km $\approx 0.2R_m$, and thus ENAs are produced all the way down to the obstacle boundary. In the MHD model on the other hand the production region is clearly separated from the planet.

The maximum of the hydrogen ENA production rate is located away from the Mars–sun line in all models, however, in the hybrid and MHD models there is a region of significant ENA production extending down to the Mars–sun line. The MHD model even shows two separated local maxima; one on the Mars–sun line and one away from it. A few quantities resulting from the different models are compared in Table 3. The total hydrogen ENA production referred to in Table 3 was calculated by integrating the ENA production within a cylinder oriented along the x-axis from $x = -3R_m$ to $x = 3R_m$, and with a radius $\rho = 3R_m$. The solar wind hydrogen ENA flux corresponds to the local maximum in the direction of the sun (at $\theta \approx 80°$) in the images with a solar zenith angle of $100°$.

Fig. 18 shows oxygen ENA images from the hybrid and MHD models, using the same colour scales for images from the same vantage point. The oxygen ENA images from the empirical model are not shown because the small amount of test
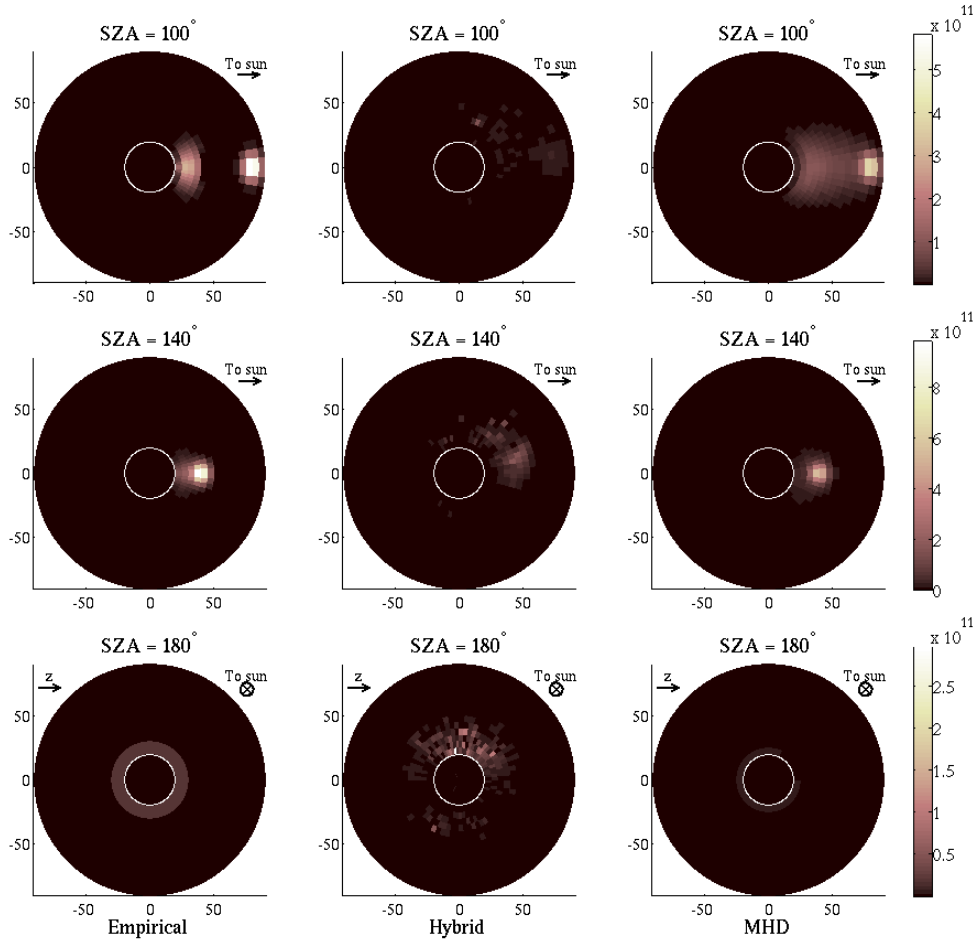
Figure 17: Hydrogen ENA images from the three models. The left column shows ENA images from the empirical model, the middle column the hybrid model, and the right column shows ENA images from the MHD model. Panels that are on the same row show images from the same vantage point, i.e. a vantage point in the $x - z$-plane, $3R_m$ from the centre of Mars, and a solar zenith angle of $100°$ (upper row), $140°$ (middle row), and $180°$ (bottom row). The colour scales are the same for panels on the same row.
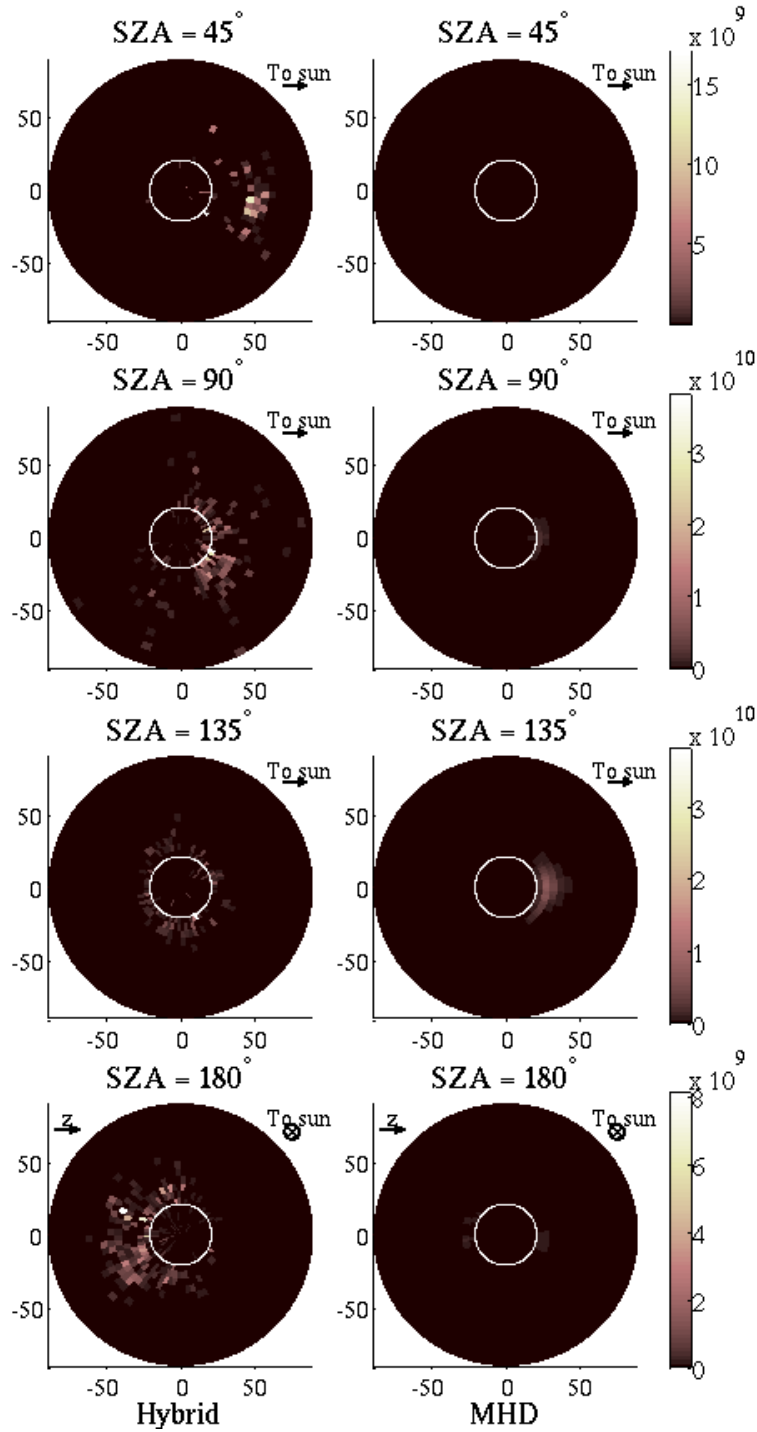
20

Figure 18: Oxygen ENA images from the hybrid (left column) and MHD (right column) models. Panels that are on the same row show images from the same vantage point, i.e. a vantage point in the $x-z$-plane, $3R_m$ from the centre of Mars, and a solar zenith angles $45°$, $90°$, $135°$, and $180°$, starting from the top row. The colour scales are the same for panels on the same row.

21

particle data available produces images that are dominated by only a few pixels, and thus are less suitable for a comparison with other models using the same linear scale. This is a problem from which also the hybrid model is suffering making the images in the left hand column of Fig. 18 more spotty than the images from the MHD model shown in the right column. The spottiness problem could be overcome in the empirical model by running a test particle simulation with a larger number of particles and in the hybrid model by using more oxygen particles or saving a larger number of files, that is dumping the positions and velocities of the ions at shorter time intervals.

In spite of the spottiness some differences between the two models can be pointed out. While the oxygen ENAs in the MHD model come mostly from the main interaction region above the subsolar point the ENAs in the hybrid model seem to come from the planet itself. This is most clearly seen in the third row of Fig. 18 that shows images from a vantage point whose solar zenith angle is $135°$. A possible interpretation of this could be that the oxygen ions that are emitted from the ionosphere in the hybrid model are dominating the ENA images. Also, in a single fluid MHD model the oxygen ions have to move in the direction of the mean plasma flow, whereas in a hybrid model oxygen ions are treated as particles and are likely to follow more realistic trajectories, the oxygen gyro-radius being of the same order of magnitude as the radius of the planet.

In the bottom row of Fig. 18 it is seen that the asymmetry of the O^+ ion density distribution in the hybrid model also is detectable in the ENA images, and that there is no such asymmetry in the MHD model. The latter fact is more clearly seen in Fig. 15. This suggests that ENA images can serve as remote measurements of asymmetries in the O^+ density distribution. The ENA flux observed from the nightside is also much higher in the hybrid than in the MHD model, which could be a result of kinetic effects that are neglected in MHD. Also in the proton density (Fig. 9) of the hybrid simulation an asymmetry is seen, which can be detected remotely using ENA images (Fig. 8).

The differences between the models regarding the O^+ density distribution and its possible dependence on the boundary conditions suggest that to make accurate predictions by the use of computer models knowledge of the boundary conditions is required.

6 Discussion

What is the best way to model the interaction between the solar wind and the Martian atmosphere? Three different models have been investigated here. The empirical model provides us with a way to compare with the measurements while these are still quite scarce. However, when we wish to perform numerical experiments in order to understand the physics behind the observations we need to use self-consistent models.

What we really would like is a three-dimensional electromagnetic particle in cell simulation that treats both ions and electrons as particles, realistically includes the interaction with the neutral gas, and resolves phenomena on both the Debye length and the planetary radius scales. Such a model is unfortunately not possible to implement at this time with the limited computer resources available in the world today.

A requirement for the applicability of MHD is that the plasma must be collision dominated. This requirement is not at all met in the solar wind nor in the neighbourhood of Mars. The use of MHD has nevertheless turned out to be successful, since there are wave phenomena and turbulence "leading to a wide variety of wave particle interactions, which in turn act as pseudocollisions" [4] in thermalising the ion distribution functions. It would, of course, be better to take these phenomena properly into account rather than simply assuming that they exist and that they influence the plasma merely by providing thermalisation.

MHD completely neglects all finite gyro-radius effects, which is particularly troublesome when ions heavier than hydrogen are important. The oxygen ions in the Martian environment have gyro-radii comparable to the size of the planet. Their motion can hardly be predicted by MHD models, and thus such models are unlikely to be sufficient for the study of oxygen ENA images. For the protons, whose gyro-radius of about $0.3R_m$, the situations is slightly better, but far from being satisfactory. Whether kinetic and finite gyro-radius effects makes MHD insufficient also for studying aspects of the solar wind-Mars interaction other than oxygen ENA images remains to be seen when more observational data is obtained.

The hybrid model studied here, like MHD, suffers from the simplifying assumption of frozen-in field lines, which is probably correct in the solar wind but may turn out to be wrong closer to Mars if the conductivity is finite. Furthermore, the results can be affected by the small number of super-particles per grid cell. It will be difficult to represent the full three-dimensional distribution function with only ten particles, and that in a very large grid cell. The grid cell size is also a problem in the hybrid simulations, no small scale phenomena can possibly be resolved. If the grid cells were to be made smaller the number of particles would have to be increased in order to keep the number of particles per cell constant.

This study also shows that not only the type of simulation code matters, but also the inclusion of relevant physical phenomena and boundary conditions. For example ionospheric emissions were included in one model but not the other. Another phenomenon that none of the models include is electron impact ionisation which could turn out to be very important. Electron impact ionisation is also likely to be affected by acceleration of electrons by waves and magnetic field-aligned electric

fields, that is, by processes that are neglected in both models.

References

[1] E. Kallio, J. G. Luhmann, and S. Barabash, "Charge exchange near Mars: The solar wind absorption and energetic neutral atom production," *Journal of Geophysical Research*, vol. 102, pp. 22183–22197, 1997.

[2] E. Kallio and P. Janhunen, "Atmospheric effects of proton precipitaion in the Martian atmosphere and its connection to the Mars-solar wind interaction," *Journal of Geophysical Research*, vol. 106, pp. 5617–5634, 2001.

[3] E. Kallio and P. Janhunen, "Ion escape from Mars in a quasi-neutral hybrid model," *Journal of Geophysical Research*, vol. 107, no. A3, 1035, doi:10.1029/2001JA000090, 2002.

[4] Y. Ma, A. F. Nagy, K. C. Hansen, D. L. DeZeeuw, and T. I. Gombosi, "Three-dimensional multispecies MHD studies of the solar wind interaction with Mars in the presence of crustal fields," *Journal of Geophysical Research*, vol. 107, no. A10, 1282, doi:10.1029/2002JA009293, 2002.

[5] M. Holmström, S. Barabash, and E. Kallio, "Energetic neutral atoms at Mars I: Imaging of solar wind protons," *Journal of Geophysical Research*, vol. 107, no. A10, 1277, doi:10.1029/2001JA000325, 2002.

[6] S. Barabash, M. Holmström, A. Lukyanov, and E. Kallio, "Energetic neutral atoms at Mars IV: Imaging of planetary oxygen," *Journal of Geophysical Research*, vol. 107, no. A10, 1280, doi:10.1029/2001JA000326, 2002.

[7] J. W. Chamberlain and D. M. Hunten, *Theory of planetary atmospheres*. San Diego, California: Academic Press, inc., second ed., 1987.

[8] V. A. Krasnopolsky and G. R. Gladstone, "Helium on Mars: EUVE and PHOBOS data and implications for Mars' evolution," *Journal of Geophysical Research*, vol. 101, no. A7, pp. 15765–15772, 1996.

[9] E. Kallio, "An empirical model of the solar wind flow around mars," *Journal of Geophysical Research*, vol. 101, pp. 11133–11147, 1996.

[10] J. Arkani-Hamed, "A 50-degree spherical harmonic model of the magnetic field of Mars," *Journal of Geophysical Research*, vol. 106, no. E10, pp. 23197–23208, 2001.